Ceramics International 43 (2017) 4462–4469

Contents lists available at ScienceDirect

Ceramics International

journal homepage: www.elsevier.com/locate/ceramint

Preparation, characterization and catalytic application of Barium molybdate ($BaMoO_4$) and Barium tungstate ($BaWO_4$) in the gas-phase oxidation of toluene

Lorena.D.S. Alencar[a,*], Alexandre Mesquita[b], Carlos A.C. Feitosa[c], Rosana Balzer[d], Luiz F.D. Probst[d], Daniel C. Batalha[e], Marcelo G. Rosmaninho[e], Humberto V. Fajardo[e], Maria I.B. Bernardi[a]

[a] Instituto de Física de São Carlos, Universidade de São Paulo, USP, 13563-120 São Carlos, SP, Brazil
[b] Instituto de Geociências e Ciências Exatas, Unesp - Universidade Estadual Paulista, Departamento de Física, 13506-900 Rio Claro, SP, Brazil
[c] Departamento de Física, Centro de Ciências Exatas e Tecnologia, Universidade Federal do Maranhão, 65080-805 São Luis, MA, Brazil
[d] Departamento de Química, Universidade Federal de Santa Catarina, 88040-900, Florianópolis, SC, Brazil
[e] Instituto de Ciências Exatas e Biológicas, Departamento de Química, Universidade Federal de Ouro Preto, 35400-000 Ouro Preto, MG, Brazil

ARTICLE INFO

Keywords:
$BaMoO_4$
$BaWO_4$
Microwave-assisted hydrothermal
Polymeric precursor

ABSTRACT

Barium molybdate and Barium tungstate are important materials due their photoluminescent properties and they also have catalysis and photocatalysis applications. In this work, powders of these compounds were prepared by microwave-assisted hydrothermal (MAH) method and polymeric precursor method (PPM) and their structural and optical properties were studied. Furthermore, these materials were employed as solid catalysts towards gas phase toluene oxidation reactions. X-ray diffraction confirms the purity of materials at both preparation methods and reveals a preferential growth when the powders are prepared by MAH due polymeric agents and processing using microwave, which was confirmed by Field emission scanning electron microscopy. Photoluminesce emission was attributed to the charge-transfer transitions within the $[WO_4]^{2-}$ and $[MoO_4]^{2-}$ complexes. The H_2 Temperature-Programmed Reduction (H_2-TPR), O_2-chemisorption and extended X-ray absorption fine structure (EXAFS) results indicated that $BaWO_4$ samples, compared with $BaMoO_4$ samples, have higher oxygen mobility and oxygen vacancies that appear as key factors for the achievement of better catalytic performances.

1. Introduction

Due to their attractive luminescence Barium molybdate ($BaMoO_4$) and Barium tungstate ($BaWO_4$) are important materials in the electro-optical industry [1]. They present general formula $BaXO_4$ (where X=Mo, W) and a scheelite-type tetragonal structure at room temperature. Belonging to the d° compounds with average wide gaps, these materials also can be envisaged as catalysts and photocatalysts either pure or doped [1].

Various methods of synthesis have been used in the preparation of these compounds [2–6], among these methods microwave-assisted hydrothermal (MAH) method and polymeric precursor method (PPM) were chosen for their synthesis in the present study.

In microwave-assisted hydrothermal method, molybdates and tungstates with scheelite-type structure are synthesized with high frequency electromagnetic radiation interacting with the permanent dipole of the solvent, which initiates a rapid heating from the resultant molecular rotation [7]. This reaction occurs in closed isolated system conditions, it is performed at pressures greater than 1 atm and temperatures above the boiling point of solvents, reducing the processing time to minutes. Therefore, microwave-assisted hydrothermal method is environmentally friendly and save energy.

Polymeric precursor method also presents significant efficiency in obtaining multi-component oxides; this process ensures the compositional homogeneity at the molecular scale due the immobilization of the metal complexes in rigid organic polymeric networks, which can reduce the metal segregation. The cation distribution throughout the entire gel system is of fundamental importance for the synthesis of multi-component oxides since the chemical homogeneity often determines the compositional homogeneity of the material [8]. Polymeric precursor method is considered low cost because the synthesis occurs at lower temperatures than those used by conventional techniques (e.g.

* Corresponding author.
E-mail address: fisicalorenaa@usp.br (L.D.S. Alencar).

http://dx.doi.org/10.1016/j.ceramint.2016.12.096
Received 27 October 2016; Received in revised form 15 December 2016; Accepted 19 December 2016
Available online 20 December 2016

solid-state reaction).

Thus, in this paper we report the preparation of $BaMoO_4$ and $BaWO_4$ samples by MAH and PPM methods and their characterization. These materials were employed as solid catalysts towards gas phase toluene oxidation reactions to demonstrate their applications. Volatile organic compounds (VOCs), such as toluene, can be harmful to the environment and human health. So, it is desirable to control the emissions of these pollutants. Catalytic abatement of VOCs has been one of the emergent technologies, mainly because of the high degradation efficiency, even in effluents with low concentrations of VOCs, and low energy cost involved [9–11].

2. Experimental

2.1. Synthesis and processing of $BaWO_4$ and $BaMoO_4$ powders by microwave-assisted hydrothermal method

In continuous stirring and heating between 70 and 90 °C, it was added to 5×10^{-3} mol of barium nitrate [$Ba(NO_3)_2$] (99% purity, Sigma-Aldrich) in 40 mL of distilled water. In another beaker, 5×10^{-3} mol of sodium tungstate dihydrate [Na_2O_4W-$2H_2O$] (99% purity, Sigma-Aldrich) or sodium molybdate dihydrate [$MoNa_2O_4$–$2H_2O$] (99% purity, Sigma-Aldrich) was diluted in 40 mL distilled water. After complete dissolution of the reagents, the solutions were mixed, and then 15 mL of ethylene glycol (EG) (99%, Synth) were added. For better dissolution of the reagents, the hydrolysis rate of system was increased adjusting the pH to 11 with the addition of 5 mL of NH_4OH (27% in NH_3, Synth). The solution remained stirring for 30 min. In the sequence, the solution was transferred to an autoclave and this was coupled to a microwave oven (2.45 GHz, maximum power of 800 W). The processing occurs at a temperature of 140 °C for 30 min and the heating rate was set at 25 °C/min. The pressure into the autoclave was stabilized at 0.34 MPa. At the end of the microwave processing, the autoclave was cooled at room temperature. The obtained suspensions were washed several times with distilled water to remove the EG and the NH_4OH, until to neutralize the pH solution (≈7) and the last wash was performed with isopropyl alcohol. The powders were dried at 80 °C for 8 h.

2.2. Synthesis of $BaWO_4$ and $BaMoO_4$ powders by polymeric precursor method

To obtain $BaWO_4$ powders, in 100 mL of distilled water under constant stirring and heating of approximately 70 °C was added 2.6×10^{-2} mol of tungstic acid [H_2WO_4] (99% purity, Aldrich) and 10 mL of NH_4OH (27% in NH_3, Synth) to adjust the pH of the solution (≈11) for complete dissolution of the tungstic acid. In another beaker, citric acid [$C_6H_8O_7$] (99.5% purity, Synth) was dissolved in 100 mL of distilled water under the same conditions of temperature and stirring. This was added to the initial solution of tungstic acid, obtaining a limpid solution (tungsten citrate). The stoichiometry between citric acid/metal used was 3:1 (molar ratio) and the molar ratio between metal cations was 1:1. Thereafter, 2.6×10^{-2} mol of barium nitrate [$Ba(NO_3)_2$] (99% purity, Sigma-Aldrich) was diluted in 100 mL of distilled water and added to the tungsten citrate. EG in a proportion (weight) citric acid/EG of 60:40 was added to promote polyesterification of the complex.

$BaMoO_4$ powders were prepared following the same procedure used for the preparation of calcium tungstate. The stoichiometry and reagents used were 3.4×10^{-2} mol of molybdenum trioxide [MoO_3] (99.5% purity, Merck) and barium carbonate [$BaCO_3$] (99.8% purity, Alfa-Aesar). However, after adding the Ba precursor, it was necessary to adjust the pH to between 2 and 3 with nitric acid [HNO_3] (65%, Synth) to avoid precipitation of the reagents. Then, EG was added.

The solutions were kept under constant stirring in a temperature range of 150–200 °C to occur the polyesterification reaction and evaporation of the excess water, obtaining clear and homogeneous resins.

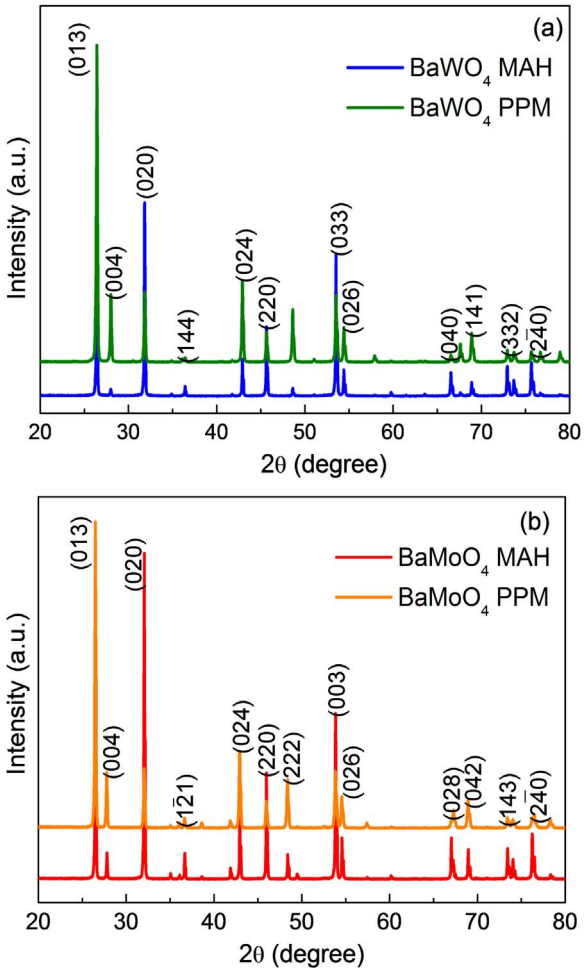

Fig. 1. XRD patterns of (a) $BaWO_4$ and (b) $BaMoO_4$ powders obtained by MAH and PPM.

The polymer resins were calcined at 300 °C for 4 h at a heating rate of 10 °C/min in ambient atmosphere, obtaining a material with porous structure due to partial decomposition of the polymer and consequent release of gas. The material obtained was deagglomerated in a mortar. The powders were calcined at 700 °C for 2 h, at a heating rate of 10 °C/min in ambient atmosphere.

2.3. Sample characterizations

BaWO4 and BaMoO4 powders were structurally characterized by X-ray diffraction (XRD) patterns recorded using a RIGAKU – ULTIMA IV X-Ray with Cu-Kα radiation (λ=1.5406 Å) in the 2θ range from 20° to 80° with a scanning rate of 0.02°/min. Field emission scanning electron microscopy (FEG-SEM) Zeiss – Sigma was employed to verify the morphology of these powders. X-ray absorption near edge spectroscopy (XANES) and extended X-ray absorption fine structure (EXAFS) measurements at the W LIII- and Mo K-edges of BaWO4 and BaMoO4 samples were collected in transmission mode as a function of the temperature using a Si(111) channel-cut monochromator at the LNLS (National Synchrotron Light Laboratory) facility. The extraction and fit of the EXAFS spectra were performed using the multi-platform applications for X-ray absorption (MAX) software package [12] and theoretical spectra were obtained using the FEFF9 code [13]. UV–Visible spectroscopy was taken with a Varian Cary −5 G. Photoluminescence (PL) spectra were taken with a Coherent Innova, with a wavelength excitation 350 nm generated by krypton ion laser

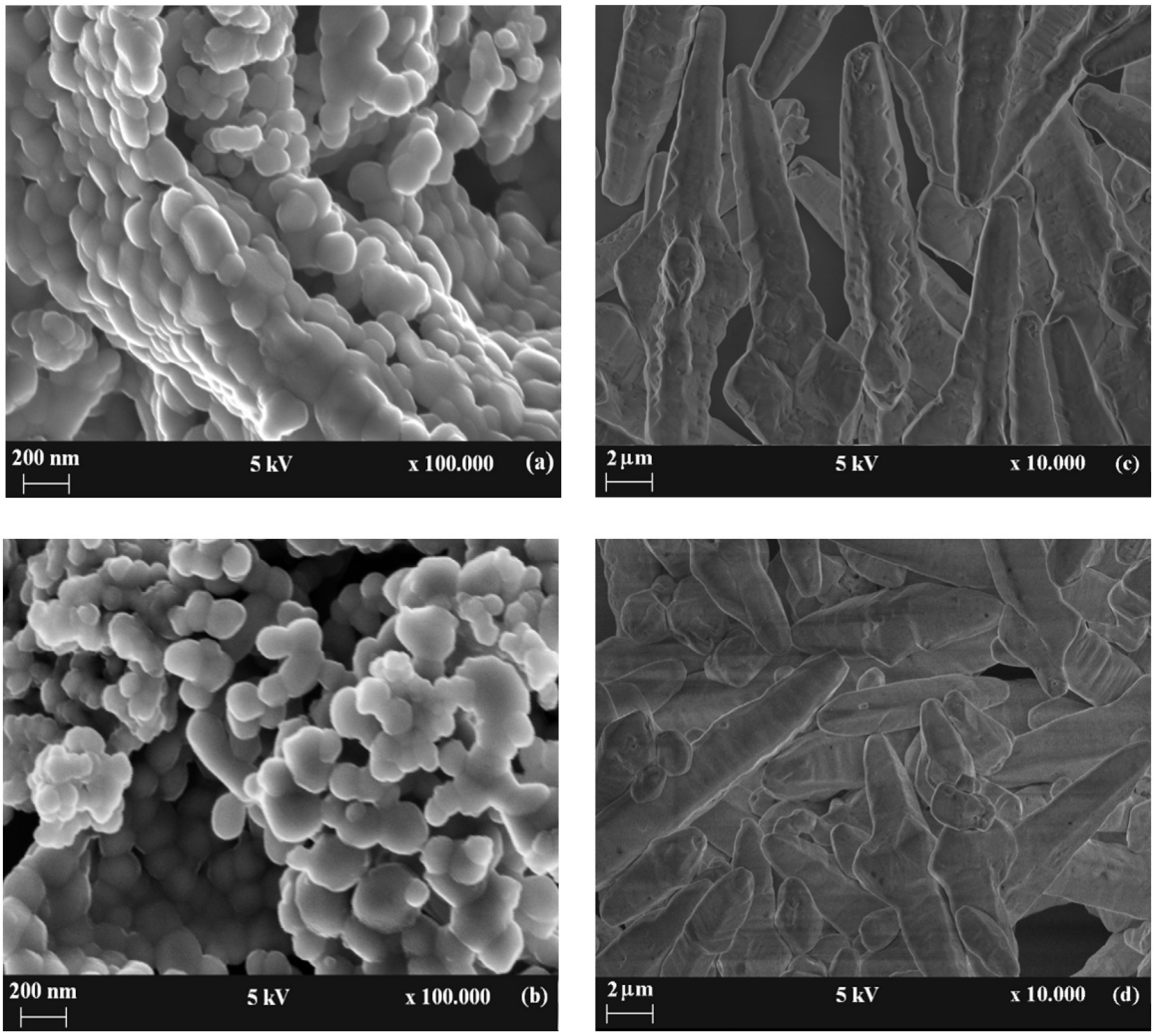

Fig. 2. FEG-SEM images of (a) $BaWO_4$ and (b) $BaMoO_4$ powders prepared by PPM and (c) $BaWO_4$ and (d) $BaMoO_4$ powders prepared by MAH method.

with adjustable output power of 200–800 mW, the width of the slit in the monochromator used is 200 nm. PL measurements were performed using a Monospec 27 monochromator (Thermal Jarrel-Ash) coupled to a R446 photomultiplier (Hamatsu Photonics) compound of a lock-in SR-530. All the above measurements were performed at room temperature. The H_2 Temperature-Programmed Reduction (H_2-TPR) was performed using a Quantachrome ChemBET-3000 instrument equipped with a thermal conductivity detector. Prior to the analysis 100 mg of the sample were packed into a quartz cell, heated for 2 h at 200 °C under a He stream and then cooled to room temperature. The experiments were performed between 25 and 950 °C in a flow of 8% H_2/N_2, the temperature increasing linearly at a rate of 10 °C min^{-1}. H_2 consumption was obtained from the integrated peak area of the reduction profiles relative to the calibration curve. CuO was used as calibration reference to quantify the total amount of H_2 consumed during the experiments. The O_2-chemisorption measurements were conducted at 600 °C using a ChemBET analyzer (Quantachrome Instruments).

2.4. Catalytic tests

The catalytic oxidation reactions of toluene were performed in a fixed-bed tubular quartz reactor, placed in an oven, under atmospheric pressure. The following conditions were chosen: 0.11 g of catalyst, inlet toluene (> 99%, Vetec) concentration 0.7 g m^{-3} in air, gas flow rate 20 $cm^3 \cdot min^{-1}$, residence time 0.3 s, gas hourly space velocity 12000 h^{-1} and temperature range 50–400 °C. The catalyst was placed in the middle of the reactor with thermocouples located on the top and bottom of the catalyst bed to monitor the reaction temperature. The catalyst was previously activated in situ under air atmosphere at 250 °C for 1 h. The reagent feed was delivered into the reactor system using a peristaltic pump (Minipuls 3 – Gilson®). The reaction data were collected after at least 2 h on stream at room temperature. The reactant and product mixtures were analyzed with two in-line gas chromatographs equipped with FID and TCD detectors and an HP-5 column. The catalytic activity was expressed as the percent conversion of toluene. The conversion of the toluene was calculated as follows: $C(\%) = \frac{[Q]_{in} - [Q]_{out}}{[Q]_{in}} x100\%$, where C(%)=percentage of toluene conversion, $[Q]_{in}$=input quantity and $[Q]_{out}$=output quantity of toluene, according to the chromatograms.

3. Results and discussion

3.1. X-ray diffraction analysis

Fig. 1 shows the XRD patterns of $BaWO_4$ and $BaMoO_4$ powders processed microwave-assisted hydrothermal method and by polymeric precursor method. The XRD patterns of $BaWO_4$ and $BaMoO_4$ powders obtained by both methods can be indexed to the scheelite-type tetragonal structure with space group $I4_1/a$ and is in agreement with the respective Inorganic Crystal Structure Database (ICSD) N° 16165

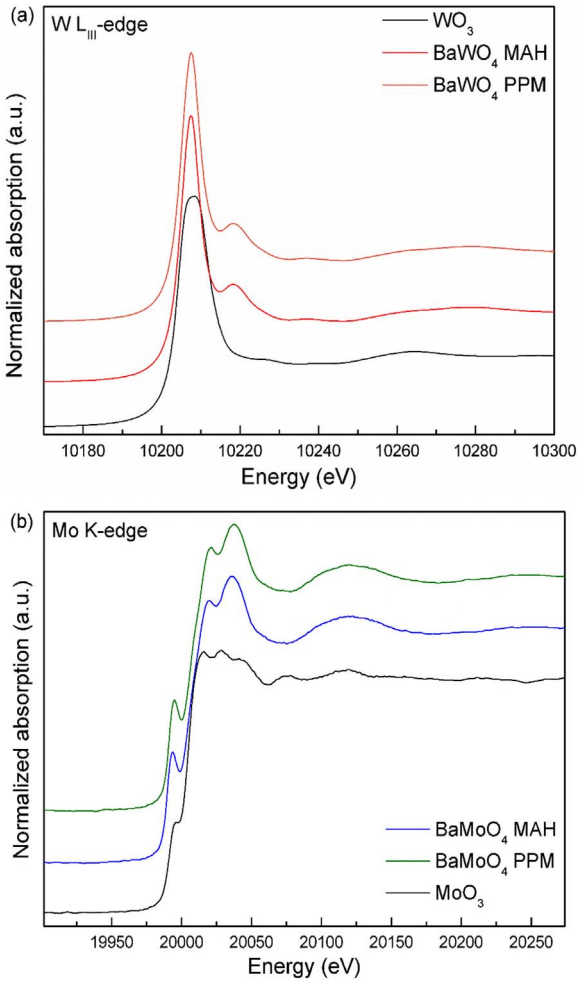

Fig. 3. XANES spectra at (a) W L_{III}-edge of $BaWO_4$ powders and at (b) Mo K-edge of $BaMoO_4$ powders.

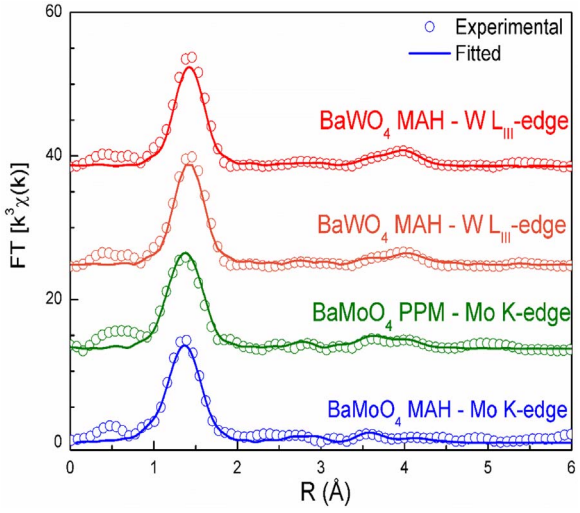

Fig. 4. Experimental and fitted modulus of k^3 weighted Fourier transform for $BaWO_4$ and $BaMoO_4$ powders at W L_{III}- and Mo K-edge, respectively. Open symbols are experimental data, and solid lines represent fittings using the parameters listed in Tables 1, 2.

for $BaWO_4$ and N° 50821 for $BaMoO_4$. For $BaWO_4$ MAH powders, XRD pattern shows high intensity diffraction peaks, related to crystallographic planes (020), (220) and (033) indicating the preferential growth in these plans, the same happens for the XRD patterns of the $BaMoO_4$ MAH powders, where the crystallographic planes (020), (220) and (003) have preferred directions. No diffraction peaks related to secondary phase were detected. X-ray patterns confirm purity of materials at both preparation methods.

3.2. Scanning electron microscope analysis

From the FEG-SEM micrographs were observed that the $BaWO_4$ PPM (Fig. 2a) and $BaMoO_4$ PPM (Fig. 2b) powders have rounded shape with agglomerated nature and average diameters of 100 nm. Fig. 2c and d show FEG-SEM micrographs of $BaWO_4$ MAH and $BaMoO_4$ MAH powders, respectively. In these figures were observed shuttle-like crystals with four prominences in the middle part, with particles sizes between 2 and 50 μm. When prepared without polymeric agents, these powders show octahedral morphology [14]. Besides the effects of polymeric agents, the type of processing using microwave is also responsible for this morphological change [5]. The anisotropic particle shape justifies the peaks observed in X-ray diffractograms which revealed preferential growth along the planes (020), (220) and (033) for $BaWO_4$ MAH and the planes (020), (220) and (003) for $BaMoO_4$ MAH.

3.3. X-ray absorption spectroscopy (XAS) measurements

The structures of the $BaWO_4$ and $BaMoO_4$ samples were also characterized by X-ray absorption spectroscopy (XAS) measurements. XANES spectra provide information on the coordination symmetry and valence of ions incorporated in a solid. The energy of the absorption edge shifts according to the valence of the absorbing ion, because the binding energy of bound electrons rises as the valence increases. Also, the shape of the absorption edge depends on the unfilled local density of states and the coordination symmetry of the absorbing element. Fig. 3a presents the XANES spectra at W L_{III}-edge for $BaWO_4$ samples and the spectrum of a WO_3 standard reference whereas Fig. 3b shows the XANES spectra at Mo K-edge for $BaMoO_4$ samples and MoO_3 standard reference.

The XANES spectra in the W L_{III}-edge of $BaWO_4$ samples, as it can observed in Fig. 3a, present different features compared to the XANES spectrum compared of the reference compound (WO_3). In these spectra, the white line mostly derives from electron transitions from the $2p$ 3/2 state to a vacant $5d$ state.[15] As the form and the shape of white line depend on the particular structure, this difference is expected because the WO_3 compound has a W atom in an octahedral environment [15]. We have observed no significant change in these XANES spectra as a function of the preparation method for $BaWO_4$ samples. It can assert that the first coordination shell around tungsten atoms is formed by four oxygen atoms in a quite regular structure independently of the synthesis conditions [15]. The similarity of the post-edge XANES spectra also indicates that second and further coordination shells are quite. Similar conclusion can be reached with the observation of Fig. 3b, which exhibits the XANES spectra at Mo K-edge for $BaMoO_4$ samples. The pre-edge peaks in XANES spectra of $BaMoO_4$ samples are attributed to the transition from Mo 1 s states to Mo $4d$, which is dipole-allowed for tetrahedral symmetry because of the hybridization with O $2p$ states [16]. The same feature results in a shoulder for MoO_3 standard compound, which presents a distorted octahedral coordination [16]. The short-range structural data provided by EXAFS offer an element-specific insight, giving quantitative information about the number, position and identity of atoms surrounding the absorbing element as well as structural disorder within the coordination spheres. Fig. 4 shows the modulus of k^3 weighted Fourier transform of $BaWO_4$ and $BaMoO_4$ samples extracted from W L_{III}- and Mo K-edge EXAFS spectra, respectively. In order to obtain quantitative information of the local structure around W and Mo atoms, Fourier transform curves were then back Fourier transformed between 1.0 and 2.0 Å to obtain the experimental EXAFS spectra to fit

Table 1
W L_{III}-edge EXAFS simulation results. R is the distance from the central atom, N is the average coordination number, σ^2 the Debye–Waller factor, and Q the quality factor.

Shell	R (Å)		N		σ^2 (10^{-2} Å^2)		Q	
	MAH	PPM	MAH	PPM	MAH	PPM	MAH	PPM
W-O	1.78 (1)	1.78 (1)	3.9 (4)	3.8 (4)	0.04 (6)	0.04 (5)	1.34	1.45
W-O	3.31(3)	3.31 (4)	2.9 (6)	2.1 (8)	1.1 (2)	0.78 (13)		
W-Ba	3.94 (2)	3.95 (3)	3.4 (5)	1.8 (7)				
W-Ba	4.23 (3)	4.23 (3)	3.4 (2)	1.8 (1.1)				
W-W	4.23 (3)	4.23 (3)	2.7 (4)	2.0 (1.1)				
W-O	5.5 (2)	6.0 (3)	1.8 (2)	1.0 (8)				
W-O	5.9 (4)	5.7 (4)	0.6 (1.5)	0.1 (5)				
W-O	4.9 (2)	5.3 (2)	0.1 (1.6)	1.0 (3.2)				

Table 2
Mo K-edge EXAFS simulation results. R is the distance from the central atom, N is the average coordination number, σ^2 the Debye–Waller factor, and Q the quality factor.

Shell	R (Å)		N		σ^2 (10^{-2} Å^2)		Q	
	MAH	PPM	MAH	PPM	MAH	PPM	MAH	PPM
Mo-O	1.72 (1)	1.76 (2)	3.9 (2)	4.1 (5)	0.21 (4)	0.12 (6)	0.78	1.13
Mo-O	3.32 (5)	3.31 (4)	4.7 (1.2)	3.7 (1.7)	1.0 (2)	0.78 (13)		
Mo–Ba	3.87 (2)	3.88 (3)	4.2 (1.1)	3.8 (1.6)				
Mo–Ba	4.25 (3)	4.20 (6)	4.3 (1.2)	4.3 (1.8)				
Mo–Mo	4.19 (4)	4.18 (6)	4.0 (9)	3.7 (1.7)				
Mo–O	4.2 (1)	3.9 (1)	3.7 (7)	3.8 (1.9)				
Mo–O	4.4 (1)	4.2 (2)	3.4 (7)	3.6 (1.7)				
Mo-O	4.8 (1)	4.7 (2)	0.0 (1.2)	1.8 (1.6)				

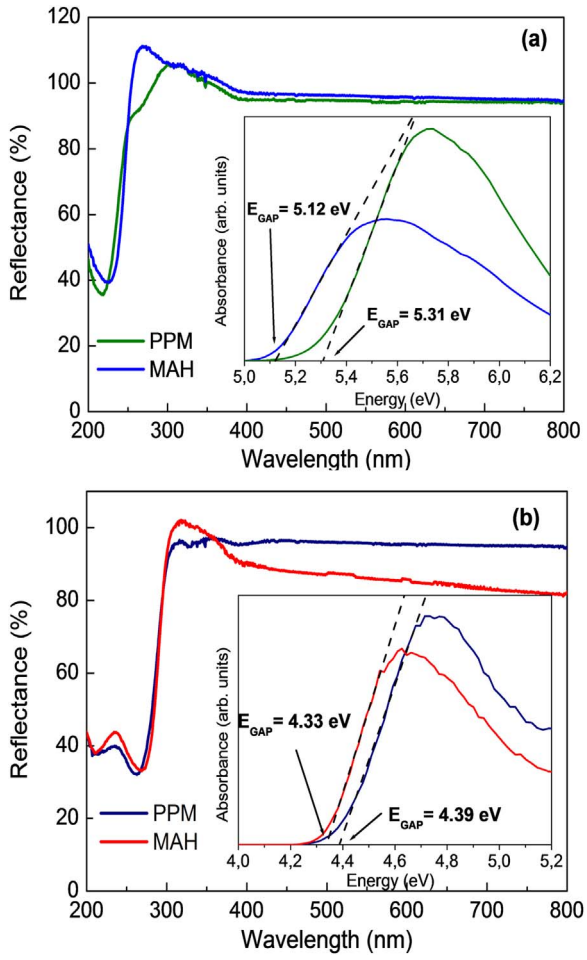

Fig. 5. UV–vis spectra of (a) $BaWO_4$ powders and (b) $BaMoO_4$ powders processed in a MAH and PPM. The insets show the obtained optical band gap for each composition.

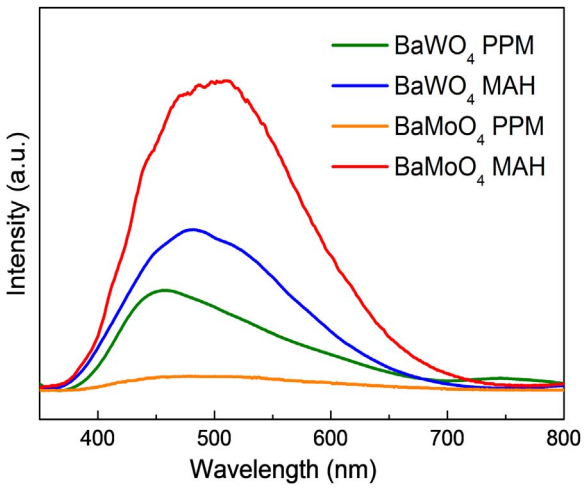

Fig. 6. PL spectra of $BaWO_4$ and $BaMoO_4$ powders (λ_{EXC}=350 nm). The maximum emission peaks are centered on 459 nm and 485 nm for $BaWO_4$, and 491 nm and 498 nm for $BaMoO_4$ prepared by MPP and HM, respectively.

using a theoretical model calculated from the FEFF9 code and crystallographic information according the XRD measurements. In all fits, the number of free parameters was kept smaller than the number of independent points, which is defined as $N_{ind}=2\Delta R\Delta k/\pi$, where ΔR is the width of the R-space filter windows and ΔK is the actual interval of the fit in the k space [17]. The reliability of the fit, determined by a quality factor (Q),57 the interatomic distances (R) and Debye–Waller factor (σ^2) relatives to the best fits are shown in Tables 1, 2.

According to the structural model, the absorber atom is surrounded by, in this order, two shells with four O atoms each, two shells with four Ba atoms each, one shell with four W or Mo atoms and three shells with four O atoms each. Thus, the more intense peak, between 1.0 and 2.0 Å in the Fourier transforms, corresponds to a single scattering interaction between the first four O atoms around the absorber atom. The single scattering interactions relative to W–Ba or Mo-Ba, W-W or Mo-Mo and W-O or Mo-O (beyond the first O neighbors) paths correspond the

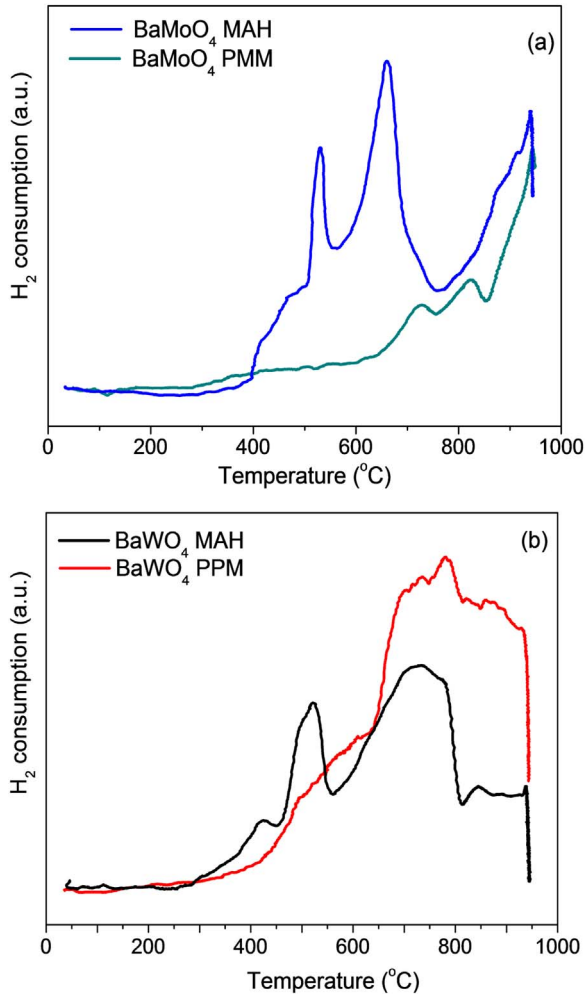

Fig. 7. H_2-TPR profiles of the catalysts: (a) $BaMoO_4$ powders and (b) $BaWO_4$ powders processed in a MAH and PPM.

region observed between 2.0 and 5.0 Å. This region also includes multiple scattering.

The extracted parameters confirm the assumption that preparation method does not introduce high order disorders into the structure. The radial distance (R) for all shells do not change considerably with the preparation method for $BaWO_4$ and $BaMoO_4$ samples. Moreover, we can trace an increase of oxygen vacancies following the average coordination number (N) for the second O-shells. Furthermore, samples prepared by the polymeric precursor method show a lower coordination number in some shells. It can suggest the presence of imperfectness in the crystal lattice. As shown by FEG-SEM micrographs, the average particle size is lower for these samples. Because of this, large amount of the atoms should be placed at the boundary of particles resulting in a lower number of neighbors [18].

3.4. UV–Visible absorption measurements

UV–vis measurements were performed in the diffuse reflectance mode and the optical band gap (E_{gap}) was estimated by method proposed by Kubelka and Munk [19,20]. Fig. 5a shows the UV–vis spectra of $BaWO_4$ powders and Fig. 5b shows the UV–Vis spectra of $BaMoO_4$ powders processed by MAH and PPM. The insets show the obtained optical band gap for each composition. The E_{gap} values obtained were 5.31 and 5.12 eV for $BaWO_4$ and 4.39 and 4.33 for $BaMoO_4$ prepared by polymeric precursor method and microwave-assisted hydrothermal method, respectively. These values are next to reported in the literature [1,21–23]; the differences in E_{gap} values of the materials studied in this work and of the values observed in the literature may be related to particle morphology, type of synthesis, time and processing temperature [4]. All these factors result in different structural defects such as oxygen vacancies and distortions on the links, which are capable of promoting the formation of intermediate energy states within the band gap [24].

The molybdates and tungstates have a typical optical absorption process characterized by direct electronic transitions occurring of maximum energy states located near or in the valence band to minimum energy states located below or in the conduction band. Due to have fewer intermediate energy levels between the valence band and conduction band these materials have a high E_{gap} value and this value is associated with the degree of order and disorder structural of the materials at an average distance [25].

3.5. PL measurements

Fig. 6 shows the PL spectra of $BaWO_4$ and $BaMoO_4$ powders prepared by the two methods proposed in this paper. Photoluminescence spectra show a broad band covering the visible electromagnetic spectrum in the range of 400–800 nm, and the profile of the emission band is typical of a multi-fonon and processes at various levels involving the participation of several states within the band gap of the material [24]. The maximum emission peaks are centered on 459 nm and 485 nm for $BaWO_4$, and 491 nm and 498 nm for $BaMoO_4$ prepared by polymeric precursor method and microwave-assisted hydrothermal method, respectively. Values close to those found in the literature, which is 542 nm to $BaMoO_4$[7] and $BaWO_4$[25]. Both materials prepared by microwave-assisted hydrothermal method show higher emission intensity when compared to materials synthesized by polymeric precursor method. The factors that influence the emission intensity are different such as processing temperature, degree of aggregation and orientation between the particles, variations in particle size distribution, particle morphology and surface defects [24].

Some authors suggest that the green photoluminescence band of barium tungstates is due of oxygen vacancies caused by distorted tetrahedral clusters $[WO_4]$ [26] and the emission of barium molybdate powders is associated with the existence of distorted $[MoO_3]$ and $[MoO_4]$ clusters, leading to the formation of intermediate energy levels within the band gap. These energy levels are basically compounds of oxygen 2p states (near the valence band) and molybdenum of 4d states (below the conduction band) [27]. But in general, these emission spectra are associated to the charge-transfer transitions within the $[WO_4]^{2-}$ and $[MoO_4]^{2-}$ complexes [21,25,28–30].

3.6. H_2-TPR measurements

Fig. 7 shows the H_2-TPR profiles of the $BaMoO_4$ and $BaWO_4$ powders. It can be observed different reducibility of the samples according to the synthesis method. The peaks represent the successive reduction steps of the Mo and W species, respectively, since the Ba reduction usually occurs at higher temperatures. For both $BaMoO_4$ and $BaWO_4$ produced by microwave assisted hydrothermal method, it can be observed signals at lower temperatures than those of the samples produced by polymeric precursor method. This suggests the presence of more oxidized species in the MAH samples. For the $BaMoO_4$ MAH sample, intense signals at about 530 and 660 °C indicate the presence of high amount of high-oxidized Mo with small particle size dispersion. For $BaMoO_4$ PMM sample it can be observed a broad and with low intensity signal starting at about 300 °C, suggesting the presence of larger particles compared to the $BaMoO_4$ MAH sample. The amount of removable oxygen atoms was considerable smaller for the sample produced by PPM route compared to the MAH material (Fig. 8b), in according with the suggested more labile oxygen removable at lower temperature. In the same way, for the $BaWO_4$ samples, the amount of

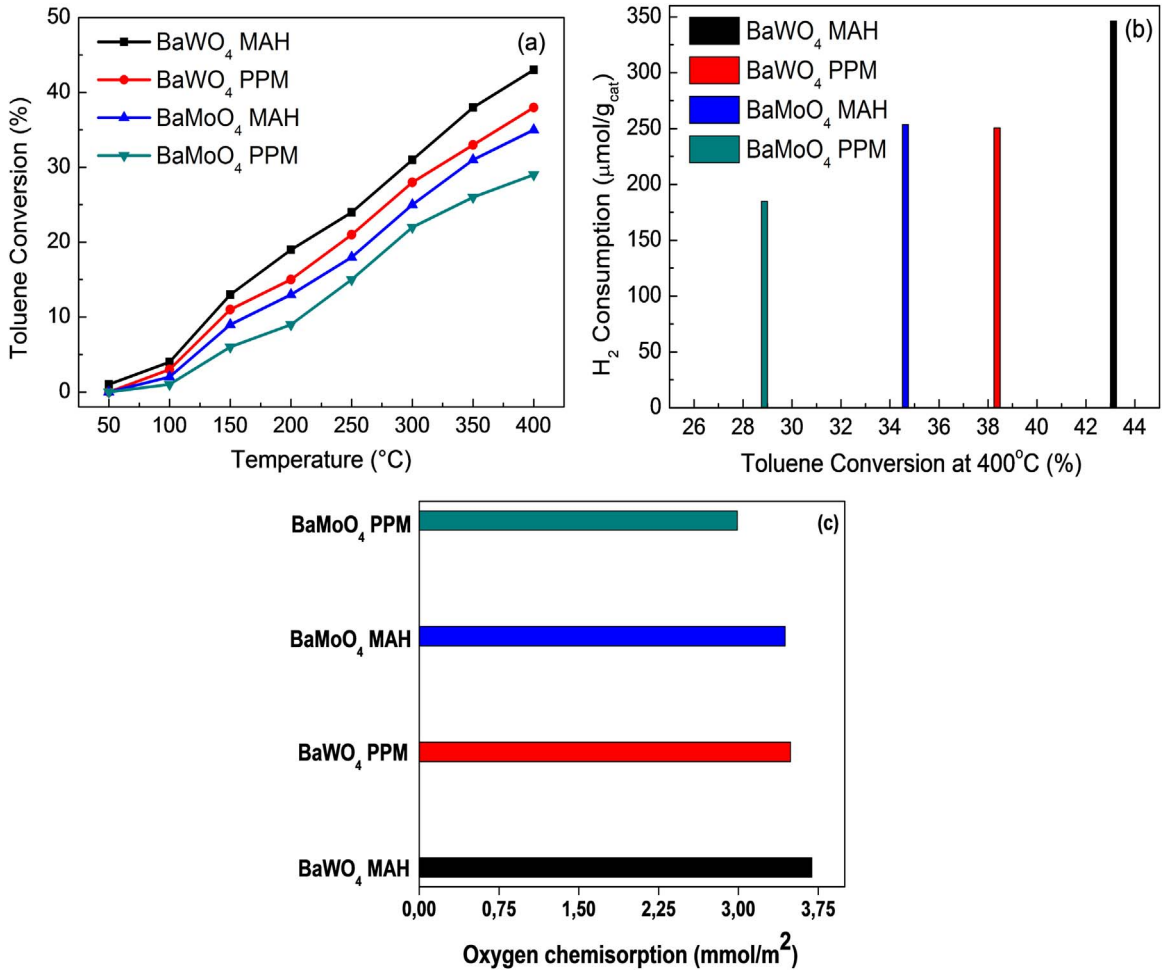

Fig. 8. (a) Toluene conversion over $BaWO_4$ and $BaMoO_4$ samples as a function of reaction temperature and (b) H_2 consumption from TPR measurements versus catalyst activity at 400 °C and (c) oxygen storage capacity (OSC) from the oxygen chemisorption measurements for each catalyst.

Table 3
Oxidation of toluene over $BaWO_4$ MAH catalyst and other catalysts reported in literature.

Catalyst	T_{30} (°C)	Reference
$BaWO_4$ MAH[a]	290	This study
1.5 wt%Au/Co_3O_4[b]	150	[40]
1.5 wt%Au/MgO[b]	295	[40]
1 wt%Au/TiO_2[c]	348	[41]
0.5 wt%Pd–1 wt%Au/TiO_2[c]	200	[41]
Cu-Mn/Al[d]	265	[42]
β-MnO_2[e]	275	[43]
Au/β-MnO_2[e]	220	[43]
1 wt%Au/TiO_2[f]	325	[44]
1 wt%Au(shell)–0.5 wt%Pd(core)/TiO_2[f]	275	[44]

[a] Gas mixture: 199ppmv in air, catalyst mass: 0.11 g.
[b] Gas mixture: 146ppmv in synthetic gas (O_2, 10 vol%; N_2, balance), catalyst mass: 0.10 g.
[c] Gas mixture: 1000ppmv in air, catalyst mass: 0.10 g.
[d] Gas mixture: 1000ppmv in air, catalyst mass: 0.225 g.
[e] Gas mixture: 2000ppmv in air, catalyst mass: 0.20 g.
[f] Gas mixture: 1000ppmv in air, catalyst mass: 0.10 g.

removable oxygen was considerable large for the MAH sample compared to the PPM sample, suggesting a presence of smaller amount of W at the sample. The broader signal for $BaWO_4$ PPM indicates a large distribution of the particle size for this material.

3.7. Catalytic activity tests

The synthesized samples were investigated as solid catalysts towards the gas-phase toluene oxidation reaction. Fig. 8a shows the toluene conversion as a function of the reaction temperature. The catalysts showed the same tendency, that is, the reagent conversion increased with the increase in the reaction temperature. The only products detected during the experiments were water and carbon dioxide. Without the catalyst, the toluene thermal oxidation started at about 350 °C and achieved only 3% conversion at 500 °C. In the presence of the catalyst, no significant conversion was detected at very low temperatures. The catalysts displayed activities from 150 °C, especially $BaWO_4$ MAH that reached almost 15% of toluene conversion at this temperature. The results showed that the toluene conversion was influenced by the type of catalyst. The $BaWO_4$ samples were more active than $BaMoO_4$ samples presenting the highest conversion levels mainly in the reaction temperatures above 150 °C. The superior oxidation performance of $BaWO_4$ samples can be ascribed to the higher oxygen mobility and oxygen vacancies, estimated by means of H_2-TPR and O_2-chemisorption measurements (higher hydrogen consumption Fig. 8b and larger oxygen uptake Fig. 8c, respectively) [31,32]. It can be inferred from Fig. 8b that the consumption amount of hydrogen varies from 346.1 μmol/g_{cat} for $BaWO_4$ MAH, the most active catalyst, to 184.8 μmol/g_{cat} for $BaMoO_4$ PPM, the less active catalyst. This indicates that the mobile oxygen species available on the $BaWO_4$ MAH surface is larger than that of $BaMoO_4$ PPM [33]. The O_2-chemisorption measurements presented in Fig. 8c also support the H_2-TPR analysis. From these values, it can be estimated the total amount

of oxygen storage capacity (OSC) available in each catalyst, which is related to the number of oxygen vacancies of them. The $BaWO_4$ MAH exhibited the largest OSC (3,69 mmol/m_2), indicating that this sample has the highest amount of oxygen vacancies [34]. The bulk and surface oxygen mobility that can be enhanced by oxygen vacancies play an important role in hydrocarbon oxidation reactions where the oxidation-reduction cycles determine the activity of the catalyst. It is commonly accepted that hydrocarbon oxidation reactions promoted by metal oxides follow a Mars-van Krevelen mechanism in which the solid oxidizes the substrate and the key steps are the supply of oxygen by the reducible oxide surface and the reoxidation of the reduced solid by the oxygen-containing gaseous phase. Oxygen vacancies on the catalyst surface can act accelerating the adsorption and dissociation of gas-phase oxygen molecules resulting in the formation of highly active O-species (e.g.,O_2^-; O_2^{2-}; O^-) that could be consumed by the organic compound. These vacancies are filled by the oxygen atoms that diffuse from the bulk to the surface of the catalyst or by di-oxygen in the air stream during the process. Thus abundant mobility of active lattice oxygen species enhanced by oxygen vacancies improves the catalytic activity in the toluene oxidation [34–39]. Table 3 shows the light-off temperature (T30, approximate temperature for the 30% toluene conversion) for toluene oxidation over the most active catalyst in the present study ($BaWO_4$ MAH) and some catalysts used in previous investigations [40–44]. It can be observed that the performance of the $BaWO_4$ MAH catalyst is comparable or superior to those of some catalysts reported in the literature, including noble metal based catalysts which are preferred for this process [45]. Although the data presented in this table have been reported using different reaction conditions, and therefore, the comparison between the catalytic behaviors must be done with precaution, they are useful to give us an idea of the good catalytic potential of the samples prepared in the present study.

4. Conclusions

$BaWO_4$ and $BaMoO_4$ powders were successfully synthesized by microwave-assisted hydrothermal method and by polymeric precursor method. XRD patterns showed that the $BaWO_4$ and $BaMoO_4$ powders have a scheelite-type tetragonal structure with space group $I4_1/a$, without diffraction peaks related to secondary phase. SEM-FEG micrographs showed that $BaWO_4$ and $BaMoO_4$ powders prepared by the polymeric precursors method present rounded shape with agglomerated nature while $BaWO_4$ and $BaMoO_4$ powders prepared by microwave-assisted hydrothermal method present shuttle-like crystals with four prominences in the middle part, with polydisperse particles sizes distribution due polymeric agents and processing using microwave. From the EXAFS results we could state that the vacancies are introduced in $BaWO_4$ and $BaMoO_4$ samples mainly for that prepared by precursor polymeric method and apparently the $BaWO_4$ samples present increased the content of oxygen vacancies relative to the $BaMoO_4$ samples. The E_{gap} value was associated with the degree of order and disorder structural of the materials at an average distance. PL emission at room temperature was attributed to the the charge-transfer transitions within the $[WO_4]^{2-}$ and $[MoO_4]^{2-}$ complexes. The H_2-TPR, O_2-chemisorption and EXAFS results indicated that $BaWO_4$ samples, compared with $BaMoO_4$ samples, have higher oxygen mobility and oxygen vacancies that appear as key factors for the achievement of better catalytic performances.

Acknowledgements

The authors gratefully acknowledge the financial support of the Brazilian research funding agencies FAPESP/CEPID (grant nos. 13/07909-4 and 13/07296-2), FAPEMIG, CAPES and CNPq. The research was partially carried out at LNLS National Laboratory of Synchrotron Light (proposal number XAFS1–19058), Brazil.

References

[1] P. Afanasiev, Mater. Lett. 61 (2007) 4622–4626.
[2] P. Parhi, T.N. Karthik, V. Manivannan, J. Alloy. Compd. 465 (2008) 380–386.
[3] D. Rangappa, T. Fujiwara, T. Watanabe, M. Yoshimura, J. Electrochem. 17 (2006) 853–860.
[4] C.S. Lim, J. Ceram. Process Res. 12 (2011) 544–548.
[5] A.P.A. Marques, F.C. Picon, D.M.A. Melo, P.S. Pizani, E.R. Leite, J.A. Varela, E. Longo, J. Fluoresc. 18 (2008) 51–59.
[6] L.S. Cavalcante, J.C. Sczancoski, R.L. Tranquilin, J.A. Varela, E. Longo, M.O. Orlandi, Particuology 7 (2009) 353–362.
[7] L.S. Cavalcante, J.C. Sczancoski, R.L. Tranquilin, M.R. Joya, P.S. Pizani, J.A. Varela, E. Longo, J. Phys. Chem. Solids 69 (2008) 2674–2680.
[8] M.A.M.A. Maurera, A.G. Souza, L.E.B. Soledade, F.M. Pontes, E. Longo, E.R. Leite, J.A. Varela, Mater. Lett. 58 (2004) 727–732.
[9] H. Huang, Y. Xu, Q. Feng, D.Y.C. Leung, Catal. Sci. Technol. 5 (2015) 2649–2669.
[10] F.I. Khan, A.K. Ghoshal, J. Loss Prev. Process Ind. 13 (2000) 527–545.
[11] F. Wang, H. Dai, J. Deng, G. Bai, K. Ji, Y. Liu, Environ. Sci. Technol. 46 (2012) 4034–4041.
[12] A.Michalowicz, J.Moscovici, D.Muller-Bouvet, K.Provost, J. Phys.: Conf. Ser.,190, 012034–012035, 2009.
[13] A.L. Ankudinov, B. Ravel, S.D. Conradson, J.J. Rehr, Phys. Rev. B: Condens. Matter 58 (1998) 7565–7576.
[14] Z. Luo, H. Li, J. Xia, W. Shu, J. Guo, B. Zhang, J. Cryst. Growth 300 (2007) 523–529.
[15] L. Gracia, V.M. Longo, L.S. Cavalcante, A. Beltrán, W. Avansi, M. Siu Li, V.R. Mastelaro, J.A. Varela, E. Longo, J. Andrés, J. Appl. Phys. 110 (2011) 043501–043511.
[16] F. Rocca, A. Kuzmina, P. Mustarelli, C. Tomasi, A. Magistris, Solid State Ion. 121 (1998) 189–192.
[17] S.S.Hasnain, Report on the international workshops on standards and criteria in XAFS, Proceedings of the VI International Conference on X-ray Absorption Fine Structures, Ellis Horwood, New York, 1991, Hor.
[18] A.L. Curcio, M.I.B. Bernardi, A. Mesquita, Phys. Status Solid 12 (2015) 1367–1371.
[19] A.E. Morales, E.S. Mora, U. Pal, Rev. Mex. Fis. 53 (2007) 18–22.
[20] P. Kubelka, F. Munk, Z. Tech. Phys. 12 (1931) 593–603.
[21] J.C. Sczancoski, L.S. Cavalcante, N.L. Marana, R.O. da Silva, R.L. Tranquilin, M.R. Joya, P.S. Pizani, J.A. Varela, J.R. Sambrano, M. Siu Li, E. Longo, J. Andrés, Curr. Appl. Phys. 10 (2010) 614–624.
[22] S.M.M. Zawawi, R. Yahya, A. Hassan, H.N.M.E. Mahmud, M.N. Daud, Chem. Cent. J. 07 (2013) 80.
[23] M.M.J. Sadiq, A.S. Nesaraj, J. Nanostruct. Chem. 05 (2015) 45–54.
[24] V.M. Longo, L.S. Cavalcante, E.C. Paris, J.C. Sczancoski, P.S. Pizani, M. Siu Li, J. Andrés, E. Longo, J.A. Varela, J. Phys. Chem. C 115 (2011) 5207–5219.
[25] L.S. Cavalcante, V.M. Longo, J.C. Sczancoski, M.A.P. Almeida, A.A. Batista, J.A. Varela, M.O. Orlandi, E. Longo, M. Siu Li, Cryst. Eng. Comm. 14 (2012) 853–868.
[26] L.S. Cavalcante, J.C. Sczancoski, L.F. Lima Jr., J.W.M. Espinosa, P.S. Pizani, J.A. Varela, E. Longo, Crist. Growth Des. 9 (2009) 1002–1012.
[27] B.M. Sinelnikov, E.V. Sokolenko, V.Y. Zvekov, Inorg. Mater. 32 (1996) 999–1001.
[28] A.B. Campos, A.Z. Simões, E. Longo, J.A. Varela, V.M. Longo, A.T. de Figueiredo, F.S. de Vicente, A.C. Hernandes, Appl. Phys. Lett. 91 (2007) (051923–051923).
[29] X. Liu, L. Li, H.M. Noh, J.H. Jeong, K. Jang, D.S. Shin, RSC Adv. 5 (2015) 9441–9454.
[30] D. Rangappa, T. Fujiwara, T. Watanabe, M. Yoshimura, J. Electroceram. 17 (2006) 853–860.
[31] L. Ilieva, P. Petrova, T. Tabakova, R. Zanella, Z. Kaszkur, React. Kinet. Mech. Catal. 105 (2012) 23–37.
[32] C.X. Zhang, S.R. Li, M.S. Li, S.P. Wang, X.B. Ma, J.L. Gong, Aiche J. 58 (2012) 516–525.
[33] G.B. Sun, K. Hidajat, X.S. Wu, S. Kawi, Appl. Catal. B 81 (2008) 303–312.
[34] R. Balzer, L.F.D. Probst, A. Cantarero, M.M. de Lima Jr, V.D. Araújo, M.I.B. Bernardi, W. Avansi Jr, R. Arenal, Humberto V. Fajardo, Sci. Adv. Mater. 7 (2015) 1406–1414.
[35] J. Li, Z. Qu, Y. Qin, H. Wang, Appl. Surf. Sci. 385 (2016) 234–240.
[36] M.H. Castaño, R. Molina, S. Moreno, Catalysts 5 (2015) 905–925.
[37] A.G.M. da Silva, H.V. Fajardo, R. Balzer, L.F.D. Probst, N.T. Prado, P.H.C. Camargo, P.A. Robles-Dutenhefner, Chem. Eng. J. 286 (2016) 369–376.
[38] Y. Liu, H. Dai, J. Deng, S. Xie, H. Yang, W. Tan, W. Han, Y. Jiang, G. Guo, J. Catal. 309 (2014) 408–418.
[39] L.F. Liotta, M. Ousmane, G. Di Carlo, G. Pantaleo, G. Deganello, G. Marcì, L. Retailleau, A. Giroir-Fendler, Appl. Catal. A 347 (2008) 81–88.
[40] H. Wu, L. Wang, Z. Shen, J. Zhao, J. Mol. Catal. A: Chem. 351 (2011) 188–195.
[41] M. Hosseini, S. Siffert, H.L. Tidahy, R. Cousin, J.F. Lamonier, A. Aboukais, A. Vantomme, M. Roussel, B.L. Su, Catal. Today 122 (2007) 391–396.
[42] L. Matejová, P. Topka, K. Jirátová, O. Solcová, Appl. Catal. A 443–444 (2012) 40–49.
[43] Q. Ye, J. Zhao, F. Huo, D. Wang, S. Cheng, T. Kang, H. Dai, Micro Meso. Mater. 172 (2013) 20–29.
[44] M. Hosseini, T. Barakat, R. Cousin, A. Aboukaïs, B.L. Su, G. De Weireld, S. Siffert, Appl. Catal. B 111–112 (2012) 218–224.
[45] L.F. Liotta, Appl. Catal. B 100 (2010) 403–412.